Absolute measurement of cellular activities using photochromic single-fluorophore biosensors

Vincent Gielen[1], Viola Mönkemöller[1], Yi Shen[2], Johan Hofkens[1], Pieter Vanden Berghe[3], Robert E. Campbell[2,4], Benjamien Moeyaert[1], Peter Dedecker[1]

[1] Department of Chemistry, KU Leuven, Belgium
[2] Department of Chemistry, University of Alberta, Canada
[3] Department of Chronic Diseases Metabolism and Ageing, KU Leuven, Belgium
[4] Department of Chemistry, University of Tokyo, Japan

peter.dedecker@kuleuven.be

Abstract

Genetically-encoded biosensors based on a single fluorescent protein are widely used to visualize analyte levels or enzymatic activities in cells, though usually to monitor relative changes rather than absolute values. We report photochromism-enabled analyte quantification (PEAQ) biosensing, a method that leverages photochromic properties of biosensors to provide an absolute measure of the analyte concentration or activity. We develop photochromic variants of the popular GCaMP family of calcium ion biosensors, and show that these can be used to resolve dynamic changes in the absolute Ca^{2+} concentration in live cells. We also show how our method can be expanded to fast imaging with reduced illumination intensities or to situations where the absolute illumination intensities are unknown. In principle, PEAQ biosensing can be applied to other biosensors with photochromic properties, thereby expanding the possibilities for fully quantitative measurements in complex and dynamic systems.

Introduction

Genetically encoded biosensors have revolutionized our understanding of the inner workings of the cell, by reporting on *in situ* enzymatic activities or the presence of a wide range of molecules such as ions, metabolites and messengers [1, 2]. Most of the genetically encoded biosensors can be divided into two classes, depending on whether their signal is read out as a change in Förster resonance energy transfer (FRET) between donor and acceptor fluorophores, or as a change in the fluorescence intensity of a single fluorophore [3]. These fluorophores are usually derived from fluorescent proteins (FPs), though other systems have also been used [4]. A key advantage of the FRET-based probes is that they can provide absolute quantification of the analyte concentration using ratiometric readout of the FRET efficiency [5–7]. However, they suffer from complications such as incomplete FP maturation [8], take up considerable spectral bandwidth, and result in relatively large genetic constructs, which complicate genome-engineering methods such as viral gene transduction. Single FP-based biosensors, on the other hand, provide fast and straightforward recording and take up less of the visible spectrum, facilitating multiplexing with other fluorescent probes or optogenetic modulators such as channelrhodopsins [9]. They are also encoded with considerably smaller genes. However, the absolute determination of the analyte concentration or activity is usually difficult to perform with these biosensors,

since their emission is affected not only by the presence of the analyte, but also by the local concentration of the probe and the illumination intensity, which depends on the nature of the sample and the depth of the imaging. Furthermore, these measurements provide no way to detect saturation of the biosensor response. This complicates the development of the *in-situ* quantitative biological models that are ultimately needed to understand and predict cell behavior.

Intriguingly, a variety of previous work has shown that the photophysical and photochemical properties of the fluorophore can reveal additional information beyond its spatial distribution. Ratiometric excitation and/or emission biosensors, for example, provide quantitative signals where the activity is encoded as the ratio between two excitation or emission bands, and have been reported both for biosensors based on FPs [10] and organic dyes [11]. However, only a limited range of single-FP biosensors has proven amenable to ratiometric operation, while organic dyes present additional challenges for the labeling of more complex samples. Fortunately, a range of other light-induced behaviors provide perspectives for innovative biosensor designs [12]. The development of photo-activatable and photoconvertible biosensors, for example, has enabled light-induced highlighting of specific features of a sample [13–16]. Other strategies have built on the use of photochromic FPs, which can be reversibly switched between a fluorescent and a non-fluorescent state through irradiation with light. Their photochromism has enabled powerful technologies such as dynamic labeling and sub-diffraction imaging [17–26]. Mechanistically, this process occurs via a light-driven cis/trans isomerization of the chromophore, followed by spontaneous (de-) protonation on account of the different pKa's of the cis and the trans state [27]. Within the field of biosensing, photochromism has been used to enable more accurate FRET quantification [28, 29], to switch between different FRET pairs in a single molecule or complex [30], to enable fluorescence lifetime imaging microscopy (FLIM)-like readout of the FRET activity using a conventional microscope [31] and as an alternative readout of homo-FRET [32]. So far, however, less work has been done on the use of these properties for biosensors based on single FPs.

Ca^{2+} is a crucial secondary messenger in many cellular processes such as neuronal signaling, muscle contraction and the regulation of cell fate. The desire to record its spatiotemporally dynamic levels *in situ* [33, 34] has led to the development of genetically-encoded Ca^{2+} indicators (GECIs) based on single FPs, which translate the intracellular Ca^{2+} concentration into a fluorescent signal [35]. Using these tools, calcium concentrations can be monitored in a variety of systems, ranging from single cells to the brain [36]. However, these studies are often limited to detecting relative changes in local calcium levels, as the quantitative assessment of these signals is limited by the intensiometric nature of single-FP GECIs. Ratiometric variants have been made by fusing a second, red-shifted fluorescent protein to the GECI, but this results in a construct that shares the limitations associated with FRET-based GECIs [37]. However, even though single FP-based GECIs are often treated as exhibiting a fluorescence signal that is solely dependent on the free Ca^{2+} concentration, previous investigations reported that the emissive signal can also depend on the previous light irradiation [15, 38]. Very recent work also showed that it is possible to engineer Ca^{2+} sensitivity into an existing photochromic protein to obtain an erasable integrator of neuronal activity [39]. We reasoned that photochromism might be utilized to obtain extra information from genetically encoded biosensors.

In this work, we set out to develop a strategy for determining absolute analyte activities using photochromic single FP-based biosensors. First, we rationally introduce mutations into GECIs to enhance their photochromic properties. The resulting reversibly switchable GECIs (rsGECIs) display photochromism that is highly dependent on the local Ca^{2+} concentration. We then demonstrate that this dependence can be used to determine the absolute Ca^{2+} concentration in cells in a way that is largely insensitive to photobleaching and the intensity of excitation light. By delivering fully quantitative information using single FP-based biosensors, we expect that our approach can be used to perform quantitative biosensing across a variety of systems.

Results and Discussion

Design of reversibly switchable GECIs

The GCaMP family is the most widely used class of single FP-based genetically-encoded Ca^{2+} biosensors [40]. They consist of a circularly permutated variant of EGFP and a Ca^{2+}-sensitive moiety made up of a calmodulin (CaM) domain and RS20, a CaM-binding peptide. Binding of Ca^{2+} ions by CaM leads to an interaction between CaM and RS20, resulting in a fluorescence increase that is largely due to a change in the pKa of the chromophore [41–43]. Well-performing photochromic variants of EGFP were previously reported [22, 44–46], which suggested that photochromic behavior might be introduced in the GCaMP biosensor design while retaining its sensitivity to Ca^{2+}.

We selected GCaMP3 [47], GCaMP6 (-s, -m, and -f variants) [48], GCaMP7s [40], and GECO1.1 and GECO-1.2 [49] as the starting scaffolds, and introduced mutations that were shown to induce photochromism in EGFP, in particular T65A, Q69L, V150A, V/A163S, and S205N (numbering according to EGFP) [22, 44]. The resulting proteins were expressed in *E. coli* and screened for brightness and reversible photoswitching with cyan and violet light (Supplementary Figures S1 to S3). We found that the single point mutation T65A or Q69L sufficed to introduce pronounced photochromism into the GECIs, while still retaining the sensitivity to Ca^{2+}, though at the cost of a reduction in overall fluorescence brightness in bacterial lysates. We attempted to improve this brightness by introducing several mutations (S30R, Y39N, N105Y, and I171V) that were previously shown to increase the expression levels of EGFP [45, 50] and GCaMP variants [51, 52]. However, these so-called superfolder mutations did not appear to influence the overall brightness in bacterial lysates and had a negative impact on the photochromism and Ca^{2+} sensitivity (Supplementary Figure S1). We therefore excluded these variants from further consideration. Based on their brightness and photochromism, we identified GCaMP3-T65A (GCaMP3-T) and GCaMP3-Q69L (GCaMP3-Q), and GCaMP6s-T and -Q as the most promising mutants, together making up a new family of reversibly-switchable genetically-encoded Ca^{2+} indicators (rsGECIs).

We next characterized their spectroscopic properties *in vitro* (Figure 1, Table 1 and Supplementary Figures S4 to S7). Overall, the absorption and fluorescence spectra are similar, although the T65A variants show a ~10 nm blue-shift in their absorption, excitation, and emission maxima. The fluorescence emission displayed Ca^{2+} sensitivities in line with those reported in literature [48] (Supplementary Figure S8).

The photochromism of each probe was then assayed in 11 different free Ca^{2+} concentrations ranging from 0 to 39 µM (Figure 1A,B and Supplementary Figure S7). The T65A or Q69L mutations clearly show enhanced photochromism over their parent proteins, where the photochromism contrast $\left((F_0 - F_{end})/F_0 = (\Delta F/F_0)_{h\nu}\right)$ strongly depends on the free Ca^{2+} concentration (Figure 1D). We obtained different K_d values for the fluorescence (Supplementary Figure S8) and the $(\Delta F/F_0)_{h\nu}$ titration (Table 1), though both titrations could be well described using a conventional sigmoidal fit. While a full analysis is outside of the scope of this contribution, this effect likely arises because the photochromism involves the contributions of multiple states, all of which can be affected by Ca^{2+} binding.

Interestingly, the $(\Delta F/F_0)_{h\nu}$ values are negative at low, but positive at high Ca^{2+} concentrations for GCaMP3, GCaMP6s, GCaMP6s-Q and GCaMP6s-T (Figure 1D and Supplementary Figure S7). This arises because these proteins show positive switching at low Ca^{2+} concentrations (cyan excitation light leads to an *increase* in fluorescence), and negative switching at higher Ca^{2+} concentrations (cyan excitation light leads to a *decrease* in fluorescence). This change in switching modalities likely results from changes in the pKa's of the fluorescent (cis) and non-fluorescent (trans) chromophore states due to calcium binding, since these determine the directionality of the switching [53].

The photochromism data (Figure 1A,B) also reveals that the first photoswitching cycle differs from all subsequent cycles, even though the illumination patterns are identical. Left in the dark, the samples recover back to the initial state following the spontaneous thermal recovery pathway, which usually takes on the

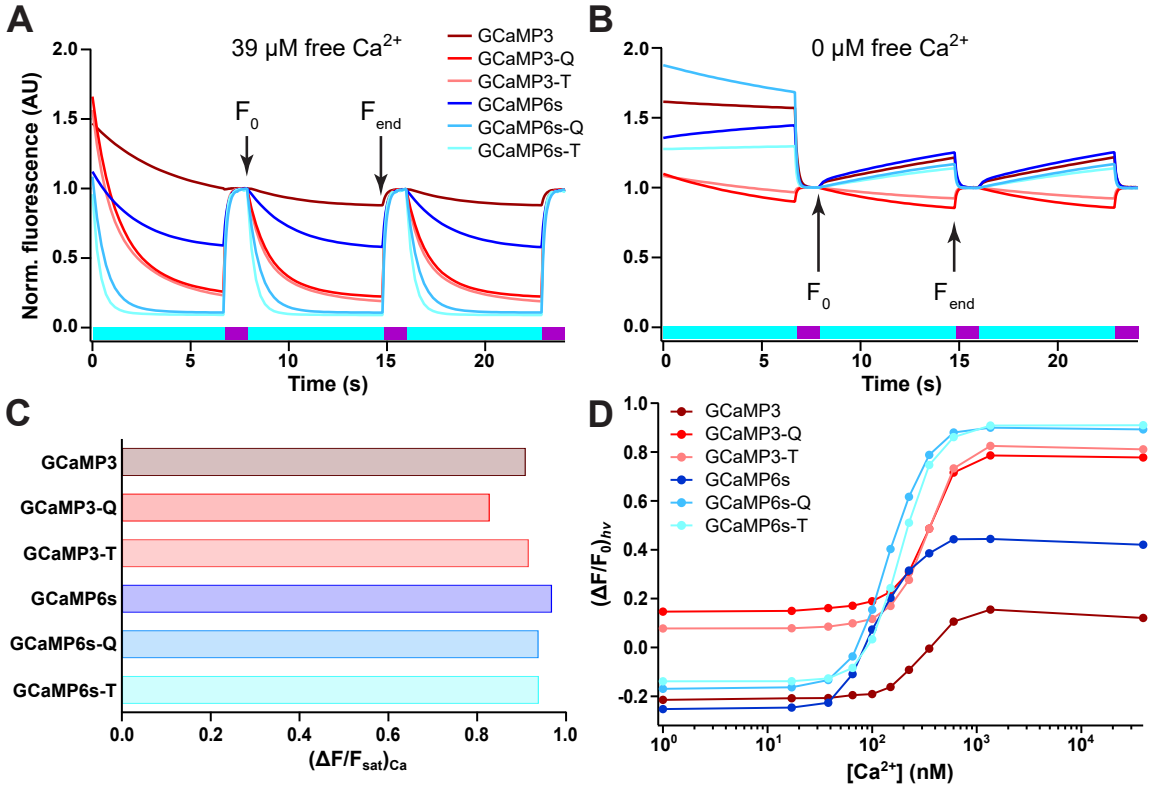

Figure 1: *In vitro* dependence of rsGECI fluorescence on light illumination and Ca^{2+}. (**A**-**B**) Cyan- and violet-light-induced photoswitching in purified rsGECI proteins in the presence (**A**) and absence (**B**) of free Ca^{2+}. The cyan and violet bars at the bottom of the plots show the sequence of the illumination. F_0 and F_{end} refer to the intensities that would be used to calculate the $(\Delta F/F_0)_{h\nu}$ values. (**C**) Fractional loss in fluorescence between 39 μM free Ca^{2+} and no free Ca^{2+}. (**D**) Photoswitching contrast ($(\Delta F/F_0)_{h\nu}$) as a function of $[Ca^{2+}]$.

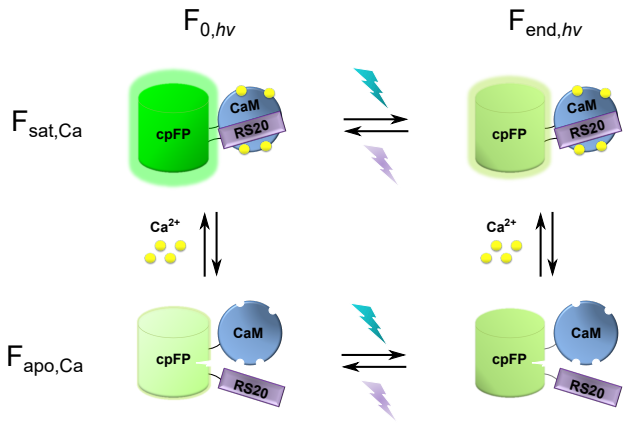

Figure 2: Schematic model for a single-FP-based rsGECI, involving the presence of four different states.

order of minutes or longer (Table 1). This phenomenon is present to a variable degree in all photochromic fluorescent proteins [54]. Successful operation of our method thus requires that an initial switching cycle is always performed at the beginning of an experiment, and discarded from the analysis.

Overall, we found that the GCaMP6s variants had an approximately 3-fold higher molecular brightness, an up to 9-fold higher Ca^{2+} response, a slightly higher photochromic contrast and a reduced pH sensitivity. Moreover, the Q69L variants have a 8- to 10-fold higher molecular brightness compared to the T65A variants. We also tested the fatigue resistance of GCaMP6s-Q, and found that it retains 70% of the original fluorescence after 300 switching cycles, while the $(\Delta F/F_0)_{h\nu}$ value was much less affected by this repeated switching (Supplementary Figure S9). As a result, we selected this protein as the best variant for our further experiments.

In summary, our measurements indicate that the rsGECIs can be represented using the scheme shown in Figure 2, consisting of four different states characterized by whether Ca^{2+} is bound and whether the molecule is in the spectroscopic on- or off-state.

PEAQ biosensing delivers absolute Ca^{2+} concentrations in live cells

We then expressed GCaMP6s-Q in HeLa cells and measured the photochromism at different Ca^{2+} concentrations, by immersing the cells in Ca^{2+}-buffered solution supplemented with ionomycin and saponin. The individual cells show pronounced responses in photochromism (Supplementary Figure S10), though displaying significant cell-to-cell variability. We found that the photochromism contrast $(\Delta F/F_0)_{h\nu}$ monotonically responded to the applied Ca^{2+} concentration, which suggested that this dependence could be used to measure absolute Ca^{2+} concentrations inside live cells. To verify this, we stimulated GCaMP6s-Q-transfected Hela cells with 25 µM histamine and measured an on-to-off switching cycle every 2 seconds (Figure 3A), obtaining absolute fluorescence intensity and $(\Delta F/F_0)_{h\nu}$ traces for each cell. Using the *in vitro* calibration curve measured using the same instrumental settings (Figure 3C), we could determine the absolute Ca^{2+} concentration at each point in the measurement (Figure 3B-D). Though the histamine-induced oscillations display high cell-to-cell variability, the magnitude of these concentrations is similar to those observed in previous work [55]. We named our approach photochromism-enabled analyte quantification (PEAQ) biosensing.

We opted to use the *in vitro* calibration as it is obtained in well-defined conditions for which the Ca^{2+} concentration is unambiguously known. The presence of cell-to-cell variability has also led to the development of *in situ* calibration schemes, in which the biosensors are driven to the unbound and fully-bound state post-

	GCaMP3	GCaMP3-Q	GCaMP3-T	GCaMP6s	GCaMP6s-Q	GCaMP6s-T
$\lambda_{\text{abs, apo}}$ (nm)	403/503	404/503	397/495	400/502	400/510	395/493
$\lambda_{\text{abs, sat}}$ (nm)	396/499	400/498	394/486	401/497	405/496	399/486
$\lambda_{\text{exc, apo}}$ (nm)	397/504	401/505	387/491	398/511	393/512	392/495
$\lambda_{\text{exc, sat}}$ (nm)	498	497	391/484	497	496	483
$\lambda_{\text{em, apo}}$ (nm)	515	515	510	518	518	512
$\lambda_{\text{em, sat}}$ (nm)	513	513	506	513	513	506
$\epsilon^{\text{app}}_{\text{apo}}$ (10^3 M^{-1} cm^{-1})	2.4	6.7	3.8	8.0	5.7	5.2
$\epsilon^{\text{app}}_{\text{sat}}$ (10^3 M^{-1} cm^{-1})	19.0	24.3	13.4	63.7	67.5	48.0
QY of fluorescence	0.59	0.29	0.10	0.60	0.34	0.07
Molecular brightness (vs EGFP)	0.33	0.21	0.035	1.13	0.69	0.083
pK_a (*sat*)	7.6	7.6	8.1	5.9	6.0	6.2
pK_a (*apo*)	10.10	8.4	8.7	12.7	10.2	11.8
K_d (nM) (Ca^{2+}, fluorescence)	549	487	550	388	519	568
K_d (nM) (Ca^{2+}, $(\Delta F/F_0)_{h\nu}$)	298	333	324	110	143	186
Hill coefficient	2.9	3.2	2.7	2.6	1.5	2.4
$(\Delta F/F_{sat})_{Ca}$ (on)	0.90	0.71	0.89	0.98	0.97	0.92
$(\Delta F/F_{sat})_{Ca}$ (off)	0.89	0.47	0.55	0.97	0.74	-0.11
$(\Delta F/F_0)_{h\nu}$ (*sat*)	-0.19	0.65	0.83	0.082	0.86	0.93
$(\Delta F/F_0)_{h\nu}$ (*apo*)	-0.44	0.39	0.31	-0.32	0.0071	-0.010
Thermal recovery, *sat* (s)	110	308	2388	38	330	726

Table 1: Spectroscopic properties of GCaMP3, GCaMP6s and their -Q and -T mutants. In the case where two values are present (e.g. 403/503), the first and second values are associated with the neutral and anionic forms of the chromophore, respectively. The extinction coefficients are 'apparent' in that they are expressed with respect to the total protein concentration, rather than purely the concentration of the fluorescent state, and are reported for the absorption maxima. Spectra and Ca^{2+} titrations are available in Supplementary Figures S1 to S8.

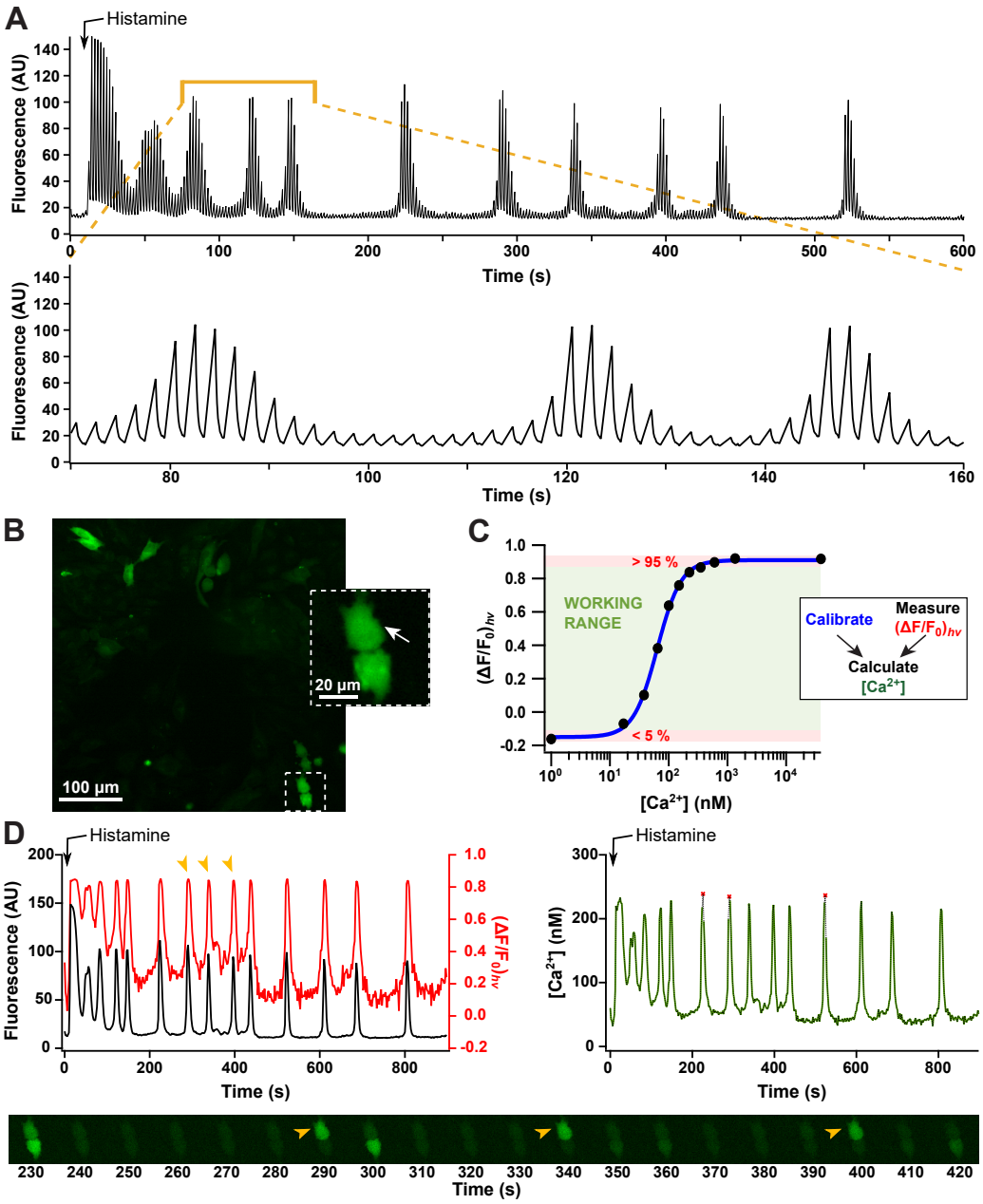

Figure 3: (**A**) Fluorescence time trace of a GCaMP6s-Q-expressing HeLa cell after stimulation with 25 µM histamine. The histamine-induced Ca^{2+} oscillations are recorded by performing a switching cycle every two seconds. The off-switching light also serves as the excitation light for imaging. (**B**) Fluorescence images of representative HeLa cells expressing GCaMP6s-Q. (**C**) Calibration curve of $(\Delta F/F_0)_{h\nu}$ at different $[Ca^{2+}]$, measured *in vitro* using the same instrumental settings as for cell imaging. The extreme 5% regions (red shading) are considered to be out of the working range (green shading). The inset to panel C shows a schematic overview of the methodology. (**D**) Fluorescence (black), $(\Delta F/F_0)_{h\nu}$ (red), and absolute $[Ca^{2+}]$ (green, right panel) traces of the cell indicated in panel B after stimulation with 25 µM histamine (arrow). Red markers represent $[Ca^{2+}]$ calculated from $(\Delta F/F_0)_{h\nu}$ values in the extreme 5% range of the calibration curve. The image sequence shows the change in fluorescence throughout a subset of the experiment. Specific time points are highlighted in the graphs and images (orange arrows).

measurement by replacement of the medium with Ca^{2+}-free and high $[Ca^{2+}]$ buffers containing ionophores and/or permeabilizing agents [5, 42, 56]. The resulting dynamic range of the signal is then used to correct the per-cell response. Our methodology should be readily compatible with this approach since the response of our system displays a similar saturation behavior in live cells (Supplementary Figure S10). However, in either case the calibration should be preferably done using instrumental settings matching those used in the actual experiment.

Our results allow us to not only determine the absolute Ca^{2+} concentration, but also to infer when the determined concentrations are less reliable due to saturation of the biosensor, a distinction that would be lost using purely intensiometric readout. We used this to visually indicate $(\Delta F/F_0)_{h\nu}$ values that fell into the upper 5% signal range of the *in vitro* calibration curve (Figure 3C). In principle, a similar consideration applies also to the lower 5% signal range, though low Ca^{2+} concentrations are more difficult to measure accurately due to the lower fluorescence emission. This could potentially be avoided entirely by using a probe in which the fluorescence change has been reduced, such as rsCAMPARI [39]. However, this strong fluorescence dependence can also facilitate hybrid measurements such as the iPEAQ measurements discussed in the following section.

Because our readout is ratiometric and does not depend on the absolute fluorescence intensities, it is less susceptible to photobleaching or dynamic changes in biosensor concentration, as was already shown *in vitro* (Supplementary Figure S9). Figure 3D, for example, shows gradually decreasing fluorescence levels that likely reflect the onset of photodestruction. However, the insensitivity of our photochromism-based readout to fluorophore concentration is reflected in the essentially constant amplitude of the $(\Delta F/F_0)_{h\nu}$ oscillations.

Combined photochromic and intensiometric measurements enable lower light doses and faster acquisitions

A possible downside of PEAQ biosensing is that a full switching cycle must be acquired for each absolute Ca^{2+} measurement (figure 4A). Switching the fluorophores to the off-state requires more time and more excitation light compared to performing a regular fluorescence acquisition, and could result in a reduced temporal resolution and more photodestruction or phototoxicity.

A key aspect of our probes is that the Ca^{2+} concentration affects both the kinetics of the photochromism and the overall fluorescence brightness of the probe. We reasoned that the cyan light dose could be reduced by alternating the on/off switching cycles with standard acquisitions of a single fluorescence image. Ordinarily, such fluorescence images do not allow the estimation of the absolute analyte concentration, since the relation between the fluorescence and the Ca^{2+} concentration depends on the probe concentration. However, we have shown that the $(\Delta F/F_0)_{h\nu}$ signal can be translated into the absolute Ca^{2+} concentration using calibration. The absolute fluorescence brightness of the probe also depends on the Ca^{2+} concentration, which can likewise be calibrated (Supplementary Figure S8). This suggests a light-efficient and fast approach to measure the absolute Ca^{2+} concentration: an initial switching cycle is performed, yielding an absolute Ca^{2+} concentration via the $(\Delta F/F_0)_{h\nu}$ calibration (Figure 4B and Supplementary Figure S11). This concentration is then used to scale the intensity calibration curve to match the brightness of the sample at the current Ca^{2+} concentration. Subsequent measurement points then measure only the fluorescence brightness. Assuming that the local probe concentration does not change, any changes in the observed fluorescence must be due to changes in the Ca^{2+} concentration, and can be similarly translated into an absolute Ca^{2+} concentration using the known $[Ca^{2+}]$-intensity relationship.

A conceptual overview of this method is shown in Figure 4B. The resulting impact on the cyan light dose is pronounced, with the total cyan light dose reducing to less than half if $(\Delta F/F_0)_{h\nu}$ acquisitions are alternated with just two regular fluorescence acquisitions (Figure 4C). The violet light dose before each acquisition can also be correspondingly reduced, since less off-switching also means that less light is required to recover

the biosensors to the fluorescent state. Finally, because measuring a single fluorescence image is faster than measuring a full off-switching event, this approach could also be used to quantitatively measure transient dynamics that occur too quickly to permit a full photochromism-based acquisition.

In principle, the switching-based calibration could be performed just once at the beginning of the acquisition, with single fluorescence acquisitions used for every timepoint thereafter. In practice, however, the local probe concentration may vary due to the dynamics of the sample, leading to fluorescence intensity changes that are not due to changes in analyte activity. A more robust approach is therefore to perform regular switching-based acquisitions alternated with a fixed number of fluorescence acquisitions, which we describe as 'intermittent PEAQ' (iPEAQ). However, one caveat of our approach is that the different K_d values for photochromism and intensiometric measurements may limit the analyte concentration window over which the calibration can be performed successfully, due to the saturation of either modality.

We verified the feasibility of this approach on HeLa cells expressing GCaMP6s-Q stimulated with histamine. Figures 4D,E and Supplemental Figure S12 show the results for a repeated sequence of eight fluorescence acquisitions between every photochromism-based calibration. Excerpts from the raw measurements are shown in Supplementary Figure S13. This procedure allowed us to reduce the cyan light exposure by 80%, while still delivering direct measurements of the absolute Ca^{2+} concentration.

PEAQ biosensing does not require knowledge of the absolute illumination intensities

The extent of the rsGECI photochromism depends not only on the Ca^{2+} concentration, but also on the intensity and duration of the cyan light. In many systems the exact excitation intensity at the sample may not be known precisely, such as when performing measurements deeper in tissues, where part of the light may be absorbed or scattered before reaching the region of interest. Such conditions also preclude the quantitative determination of the activity using purely intensiometric measurements, even if the probe concentration were known. We therefore investigated whether our method could be used reliably when the absolute excitation intensity is unknown.

Our key observation is that the fluorescence cannot be suppressed completely through irradiation with off-switching light, but instead reaches a plateau that reflects an equilibrium between the on- and off-switching of the fluorophore. Because both the initial fluorescence intensity and the plateau scale with the applied light intensity (Figure 5A), the resulting $(\Delta F/F_0)_{h\nu}$ values are largely independent of the excitation intensity (Supplementary Figure S14). Provided that the applied light dose is sufficient to approach the plateau, which can be verified by monitoring the evolution of the fluorescence in time, the resulting measurements do not require knowledge of the absolute illumination intensities. Alternatively, the level of the plateau can be extrapolated by fitting each of the acquired switching cycles with an exponential function (Figure 5B). To verify this approach, we measured photoswitching in 11 different Ca^{2+} concentrations in a representative HeLa cell at 47 mW and 24 mW excitation power (Figure 5C). Values for $(\Delta F/F_0)_{h\nu}$ were independent of the method of choice and yielded very similar $[Ca^{2+}]$ over a range of excitation intensities (Supplementary Figure S14). This finding makes it possible to apply our method also in more complex samples.

Conclusions

We have demonstrated a novel approach for the imaging of absolute cellular activities using photochromic single FP-based biosensors, which we call photochromism-enabled absolute quantification (PEAQ) biosensing. Starting from the GCaMP family of Ca^{2+} biosensors, we showed how pronounced photochromism could be introduced using a limited set of mutations. We found that the single point mutations T65A or Q69L were sufficient to gain a 10-fold improvement in photochromism contrast, and determined that these mutants retained their strong sensitivity to the local Ca^{2+} concentration. We found that the combination of GCaMP6s

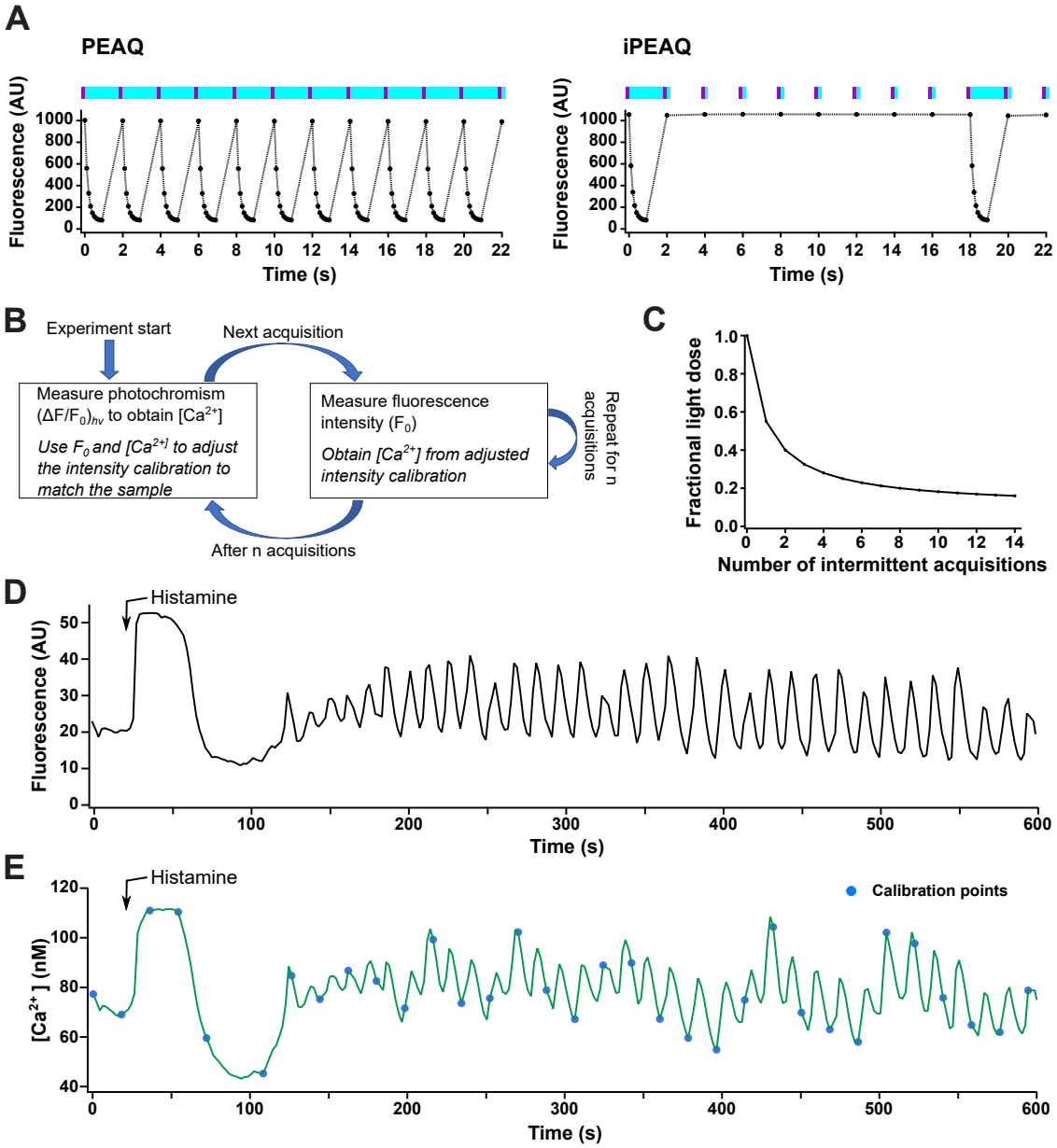

Figure 4: PEAQ biosensing with intermittent calibration. (**A**) Comparison of the irradiation procedure of PEAQ biosensing with continuous photoswitching (left), and PEAQ biosensing using intermittent calibration points (right). (**B**) Schematic overview of the intermittent calibration methodology. (**C**) Fraction of the light dose that can be saved using iPEAQ as a function of the number of intensiometric acquisitions per photoswitching cycle. (**D**) Fluorescence intensity (F_0) of a single GCaMP6s-Q-expressing HeLa cell after stimulation with 25 µM histamine. (**E**) Graph showing the Ca^{2+} concentration calculated using the calibration $(\Delta F/F_0)_{h\nu}$ values (blue markers), together with the F_0-based interpolation (green).

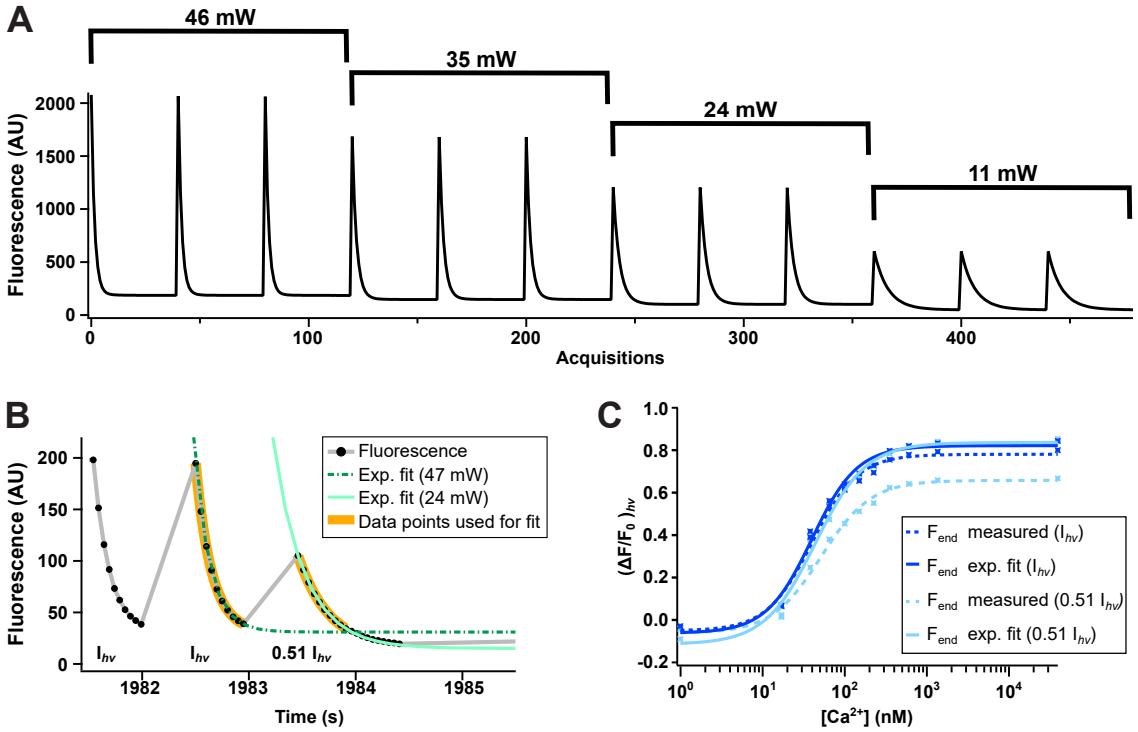

Figure 5: Intensity-independence of PEAQ biosensing. **A**: Raw fluorescence traces obtained on purified GCaMP6s-Q protein at 39 µM free Ca^{2+} with varying powers of cyan irradiation. Full data including other Ca^{2+} concentrations is shown in Supplementary Figure S14. **B**: Raw fluorescence trace (black) of a representative GCaMP6s-Q-expressing Hela cell at high Ca^{2+} concentration during photoswitching. Off-switching was achieved via either 10 acquisitions with 47 mW cyan excitation ($I_{h\nu}$), or 20 acquisitions with 24 mW cyan excitation (0.51 $I_{h\nu}$). Green dashed lines show the exponential fits of the off-switching decays. The thick orange bands indicate the 10 data points used for fitting. **C**: Ca^{2+} titration of GCaMP6s-Q expressed in a representative HeLa cell. $(\Delta F/F_0)_{h\nu}$ was calculated using either F_{end} measured after ten acquisitions, or an F_{end} parameter obtained from the plateau of an exponential fit. Dark hues are used for responses obtained with 47 mW excitation, lighter hues for 24 mW excitation. For the dashed curves, $(\Delta F/F_0)_{h\nu}$ was calculated using the F_0 and F_{end} intensities from the background-corrected traces. For the solid curves, $(\Delta F/F_0)_{h\nu}$ was determined using F_0 and the F_{end} parameter from the exponential fit.

with Q69L yielded the most promising performance, and named this mutant GCaMP6s-Q.

The Ca^{2+} concentration not only affected the overall fluorescence brightness but also altered the photochromic properties of the biosensor. We quantified the extent of the photochromism by measuring the fluorescence before and after illumination with cyan light, providing a metric that is conceptually straightforward and easily measured. *In vitro* calibration of $(\Delta F/F_0)_{h\nu}$ versus $\left[Ca^{2+}\right]$ allowed us to determine the absolute concentration of Ca^{2+} in solution.

We then demonstrated the measurement of intracellular Ca^{2+} concentrations in live HeLa cells stimulated with histamine, enabling us to follow a diverse range of Ca^{2+} dynamics. Our approach not only allowed the measurement of absolute Ca^{2+} concentrations, but also made it possible to determine when these results are less reliable due to saturation of the biosensor, and is independent of changes in local probe concentration that may occur through sample dynamics or photodestruction.

A possible downside of PEAQ biosensing is that inducing the photochromism involves more irradiation and is slower compared to the acquisition of a single fluorescence image, increasing the chance of phototoxic effects and making it more difficult to resolve fast dynamics. In response, we developed iPEAQ, a scheme in which quantitative photochromism-based measurements are alternated with one or more regular fluorescence acquisitions. Ordinarily, such intensity-based acquisitions do not permit the quantitative determination of the biosensor activity. However, we showed that absolute quantification can be achieved for both types of acquisitions, by leveraging the dependence of both the photochromism and the fluorescence brightness on the Ca^{2+} concentration. In principle, a single photochromism-based reference measurement is sufficient to enable fast quantitative measurements for the entire duration of the experiment, though in practice periodic photochromism-based measurements are likely required to adapt to the dynamics of the sample. The ability to introduce a non-invasive reference measurement at any time is a key advantage of our method.

Many experimental scenarios require measurements in more complex samples such as tissues, where the absolute intensity of the excitation light is typically not known due to the absorption and scattering. We find that our method does not require knowledge of the absolute excitation light intensity, provided that the measurements are performed in such a way that the photochromism is allowed to go to a level where the on- and off-switching are in equilibrium, or to a level where this equilibrium can be estimated. This can be readily verified, even if the absolute intensity is unknown, by monitoring the fluorescence response to the illumination. This approach is also fully compatible with the reduced light doses afforded by our alternating photochromism- and intensity-based measurements, and should allow our method to scale to a broad variety of samples and settings.

As it utilizes a single FP-based biosensor and ratiometric readout, our method is also less sensitive to issues such as limited FP maturation or photodestruction, while also being readily amenable to the multiplexing of multiple biosensors emitting in different wavelength bands. We also expect that our methodology can be applied to any FP-based biosensor that displays, or can be engineered to display, photochromism, including the many GCaMP-like biosensors that have been developed. Overall, our work readily extends the possibilities for fully quantitative measurements inside complex systems.

Acknowledgements

We thank Sam Duwé, Wim Vandenberg, Hideaki Mizuno (KU Leuven) and Alison Tebo (ENS Paris) for critical comments and insightful discussion. We thank Beatrice Adelizzi, Thomas le Saux, and Ludovic Jullien (ENS Paris) for critical comments and insightful discussion related to the acquisition methodology and data analysis. We thank Thijs Roebroek (KU Leuven) for assistance with the imaging. We thank Abhi Aggarwal (University of Alberta) for technical assistance and helpful discussion. V.G. thanks the Research Foundation Flanders (FWO Vlaanderen) for a doctoral fellowship. B.M. thanks the Research Foundation Flanders for a postdoctoral fellowship. Work in the lab of R.E.C. was supported with funding from the University of Alberta

and the Natural Sciences and Engineering Research Council of Canada (RGPIN-2018-04364). This work was supported through funding from the Research Foundation Flanders through grants 1514319N, G090819N, G0B8817N, and the European Research Council through grant 714688 NanoCellActivity.

Author contributions

P.D. designed and supervised research. V.G., V.M., B.M., and P.D. designed experiments. V.G., V.M., and B.M. performed experiments. V.M. performed analysis of the cell-based experiments. V.G., V.M. and B.M. performed analysis of the in vitro experiments. Y.S. identified the T65A mutation and edited the manuscript. R.E.C. supervised research on the T65A mutation and edited the manuscript. P.V.B. contributed ideas, discussions and advice concerning ratiometric calcium measurements in live cells. J.H. contributed critical insights and discussion. V.G., V.M., B.M., and P.D. wrote the manuscript with input from all authors.

Competing interests

The authors declare no competing interests.

Methods

Cloning and Site-Directed Mutagenesis

For expression in *E. coli*, GCaMP3, 6s, 6m, 6f, 7s, GECO1.1 and GECO1.2 were cloned in a pRSET B vector and mutations were introduced using a modified QuikChange protocol [57]. Eukaryotic expression vectors were created by inserting PCR-amplified (rs)GECI genes between BamHI and EcoRI restriction sites of a pcDNA3 vector. Primers were ordered at Integrated DNA Technologies and all constructs were verified by DNA sequencing (LGC Genomics).

Bacterial Cell Lysate Screening

The (rs)GECIs were transformed into JM109(DE3) competent cells (Promega) and incubated at 37°C. The next morning, colonies were inoculated into 1.2 mL of LB media supplemented with ampicillin in 96 deep-well blocks. Cultures were grown at 30°C for 36 h, then harvested by centrifugation at 4000 rpm for 20 minutes at 4°C, frozen, thawed, resuspended in 500 µL lysis buffer (100 mM MOPS, 100 mM KCl, 1 mg/mL lysozyme, pH 7.4), and subsequently incubated at 30°C for 1 h while shaking. Cell debris was pelleted by centrifugation at 4000 rpm, and 95 µL clarified lysate was transferred to a 96-well fluorescence microplate (Greiner). The cell lysate samples were mixed with EGTA to a final concentration of 1 mM, and fluorescence was measured at 490 nm excitation and 530 nm emission (Tecan Safire II, bandwith 20 nm, gain 40 V). Subsequently, $CaCl_2$ (5 mM final concentration) was added to the lysates and the fluorescence was measured again.

The photoswitching was measured on an Olympus IX71 inverted microscope equipped with a Spectra X Light Engine (Lumencor), a 10× UplanSApo objective (Olympus), a ZT488RDC dichroic mirror and ET525/30m emission filter (both Chroma) and an ORCA-Flash4.0 LT+ sCMOS camera (Hamamatsu). Lysates were switched off in 30 steps of 250 ms with cyan light (32 mW) and switched back on in 30 steps of 50 ms with violet light (12 mW). After each step an image was acquired with a camera exposure time of 20 ms and 10 mW cyan excitation light.

The rsGECIs with the T65A mutation were discovered during an independent and parallel effort. This effort aimed to produce a rsGECI by grafting the reversible-switching rendering mutations of rsEGFP and rsEGFP2 [22, 44] onto the GFP-based GECI, GCaMP6s [48]. Towards this end, a bacterial expression plasmid pBAD-GCaMP6s was first created by PCR amplification of the GCaMP6s gene from pGP-CMV-GCaMP6s (Addgene Plasmid #40753), followed by a Gibson Assembly (New England Biolabs) reaction with the PCR product and an XhoI/HindIII-digested pBAD/His-B vector (Thermo Fisher Scientific). Using pBAD-GCaMP6s as the template, five separate primers, each encoding a mutation from rsEGFP or rsEGFP2 (T65A, Q69L, V150A, V163S, or S205N, numbered according to EGFP), were pooled together and used to perform multi-site mutagenesis using the QuikChange Multi site-directed mutagenesis kit (Agilent). Due to imperfect reaction efficiency, this procedure was expected to introduce all five single mutations and all possible combinations of multiple mutations. The resulting plasmid library was used to transform DH10B electro-competent cells (Thermo Fisher Scientific). Transformed bacteria were plated on LB-agar plates and incubated overnight at 37°C. A total of 48 green fluorescent colonies were picked from the plates and cultured in 5 mL LB media with ampicillin and arabinose at 37°C overnight. Bacteria were pelleted by centrifugation and soluble cell lysates were extracted using Bacterial Protein Extraction Reagent (B-PER, Thermo Fisher Scientific). Lysates were then screened for photochromism. Briefly, bacterial lysate samples in clear PCR tubes were illuminated for 10 seconds using a custom-built bacterial colony fluorescence imaging macroscope [58] to either switch-on (violet light, 405/40 nm) or switch-off (cyan light, 470/40 nm) the protein fluorescence. The fluorescence change was assessed by visual inspection, and samples exhibiting photochromic behavior were immediately transferred to a multi-well plate to record the fluorescence excitation and emission spectrum using a fluorescence plate reader (Tecan). Of the 48 colonies screened, two photoswitchable variants were identified: GCaMP6s-T65A and GCaMP6s-Q69L/S205N. Later effort focused on the T65A mutant due to its more pronounced photoswitching contrast.

Spectroscopy of Purified Proteins

Proteins were purified largely following our previously described method [45]. The purified proteins were diluted in 30 mM MOPS, 100 mM KCl, pH 7.2 (Calcium Calibration Buffer #1, C3008MP, Thermo Fisher Scientific) containing either 10 mM CaEGTA (39 μM Free Calcium Buffer) or 10 mM EGTA (Zero Free Calcium Buffer). Fluorescence excitation and emission spectra were measured on an Edinburgh 920FLS fluorimeter with 1.5 nm slits. Excitation spectra were taken from 300 to 515 nm, with emission at 520 nm. Emission spectra were taken from 485 to 700 nm, with excitation at 480 nm. Spectra were normalized to the calcium-saturated excitation and emission maxima, respectively. Absorption spectra were taken on a UV/VIS spectrometer (Ocean Optics USB4000, Ocean Insight), and normalized using the absorbance at 280 nm.

In vitro Ca^{2+} Titrations

Ca^{2+} affinity assays were performed by employing a reciprocal dilution method with the Calcium Calibration Buffer Kit #1, according to the manufacturer's instructions (C3008MP, Thermo Fischer Scientific). A small aliquot of the stock protein solution was added to 2 mL of the Zero Free Ca^{2+} Buffer (10 mM EGTA, 100 mM KCl, 30 mM MOPS, pH 7.2) to create the "zero Ca^{2+} sample." The "high Ca^{2+} sample" was prepared by diluting exactly three times as much protein into 6 mL of 39 μM Free Ca^{2+} Buffer (10 mM CaEGTA, 100 mM KCl, 30 mM MOPS, pH 7.2). The initial 0 mM CaEGTA/GCaMP sample was loaded in the cuvette, and absorbance and emission spectra were recorded. Consecutively, the measured sample was used to prepare the next solution by removing a given volume from the sample and replacing this with an equal aliquot of the "high Ca^{2+} sample". Removed aliquots were stored overnight at 4°C. The next morning, all aliquots were transferred to a 96-well fluorescence microplate, and measured on the Olympus IX71 microscope (ZT488RDC, ET525/30m, 10× UplanSApo, Lumencor Spectra X light source) to evaluate the Ca^{2+}

dependence of $(\Delta F/F_0)_{h\nu}$. We subjected each well to three off/on photoswitching cycles. From these, the $(\Delta F/F_0)_{h\nu}$ was calculated as $(F_0 - F_{end})/F_0$ with F_0 the fluorescence read at the first frame of the second off-switching cycle and F_{end} the last frame of the second off-switching cycle (Figure 1A and B). The proteins were submitted to three switching cycles in which they were switched off in 30 steps of 200 ms with cyan light (10.9 mW) and switched back on in 30 steps of 10 ms with violet light (16.4 mW). Images were recorded with 10.9 mW cyan excitation and 30 ms exposure time.

Spectroscopic characterization

Spectroscopic properties of the rsGECI variants were investigated in buffer solutions in the absence (*apo*) or presence (*sat*) of free Ca^{2+}. Further spectral analysis (absorbance and emission) of calcium titrations, and respectively, photoswitching, thermal recovery, and the quantum yield of fluorescence, all in *apo* and *sat*, were measured on a home-built setup described elsewhere [59].

The GCaMP6s-Q photoswitching fatigue was measured on the Olympus IX71 microscope (ZT488RDC, ET525/30m, 2× UplanSApo, Lumencor Spectra X light source). Purified GCaMP6s-Q protein was diluted in 39 µM Free Calcium Buffer and transferred to a 96-well plate. The well plate was covered to prevent evaporation. The protein was completely switched off in 30 steps of 1 s cyan irradiation (46.7 mW), and switched back on in 30 steps of 0.1 s violet irradiation (59.3 mW). This cycle was repeated 300 times to determine the decrease in on-state fluorescence (F_0) and photoswitching contrast $(\Delta F/F_0)_{h\nu}$ after repeated switching. Images were recorded with 32 mW cyan excitation and 100 ms exposure time.

Extinction coefficients (ϵ_{apo} and ϵ_{sat}) were determined according to Ward's method[60] using the literature values of EGFP, GCaMP3 and -6s as references. Quantum yield (QY) was determined relative to EGFP, having a QY of 0.6 [61]. Molecular brightness was defined as the product of ϵ_{sat} and QY, scaled to a value of 100 for EGFP.

pH titrations were performed in a universal buffer consisting of 50 mM citrate, 50 mM Tris, 50 mM glycine, 100 mM NaCl, and either 5 mM $CaCl_2$ ($pK_{a,\,sat}$) or 5 mM EGTA ($pK_{a,\,apo}$). Absorbance spectra were measured on a Varioskan LUX Multimode Microplate Reader at pH values ranging from 4.5 to 10.5 and a plot of the absorption maxima of the anionic form in function of the pH was fitted to a sigmoid curve to yield the pKa.

Cell Culture

HeLa cells cells were cultured in DMEM supplemented with 10% FBS, glutaMAX, and 0.1% gentamicin (all Gibco) at 37°C and 5% CO_2. Before transfection, cells were seeded in 35 mm glass bottom dishes (MatTek), and allowed to settle between 4 h and 24 h. Cells were transfected using the FuGENE 6 Transfection Reagent (Promega) at a ratio of 1 µg DNA/3 µL FuGENE 6 according to the manufacturer's protocol. Cells were supplied with fresh growth medium after 24 h, and imaged 48 h after transfection.

Microscopy in Mammalian Cells

For imaging, cells were rinsed twice and maintained in Hanks' Balanced Salt Solution (HBSS; Invitrogen), supplied with 20 mM HEPES and 2 g/L D-glucose at pH 7.4 (HHBSS). Comparable solutions were made without Ca^{2+} and Mg^{2+}, but with all other components (HHBSS(-)). All imaging experiments were performed on the Olympus IX71 microscope previously described.

For the Ca^{2+} titration in HeLa cells, the cells were washed twice and kept in HHBSS(-). Subsequently, a 2× stock solution of EGTA/ionomycin was added to the cells to a final concentration of 3 mM EGTA and 5 µM ionomycin, followed by incubation at room temperature for 10 minutes. Then, the buffer was replaced with ionomycin- (5 µM) and saponin- (0.005%) supplemented Zero Free Ca^{2+} Buffer, and acquisition was started

immediately. Three photoswitching cycles were recorded every 90 seconds. The medium's Ca^{2+} concentration was changed every 180 seconds through a reciprocal dilution of 10 mM CaEGTA buffer (supplemented with 5 µM ionomycin and 0.005% saponin) into the Zero Free Ca^{2+} Buffer, according to the manufacturer's protocol (Ca^{2+} Calibration Buffer Kit #1). The proteins were switched on using a single 100 ms pulse of violet light (59.3 mW), while off-switching was achieved by acquiring 10 images with 46.7 mW of cyan excitation light and a camera exposure time of 100 ms.

For the imaging of histamine-induced Ca^{2+} dynamics, cells were imaged for a duration of 15 minutes during which the GCaMP6s-Q was switched on (100 ms pulse of 59.3 mW violet light) and off (10 acquisitions, 46.7 mW cyan light, 100 ms exposure time) every 2 s. Cells were washed twice with regular HBSS, and approximately 15 s after the start of the experiment, histamine (50 µL) was added to the cells to a final concentration of 25 µM. To determine $\left[Ca^{2+}\right]$ during histamine-induced dynamics, a $(\Delta F/F_0)_{h\nu}$ titration curve has to be measured *in vitro* under exactly the same settings as for the actual experiments.

Power independence

Measurements *in vitro* and in HeLa cells were performed as described previously. Cyan powers used for excitation were 10.9 mW, 23.8 mW, 35.4 mW, and 46.2 mW as measured at the top of the objective.

Data analysis

All data analysis was done using IgorPro 8.0 (Wavemetrics). Titration curves were fitted with the following Hill equation:

$$f\left(\left[Ca^{2+}\right]\right) = F_{\text{diff}} \cdot \left[1 - \left(\frac{\left[Ca^{2+}\right]^h}{{K_d}^h + \left[Ca^{2+}\right]^h}\right)\right] + F_{\max} \tag{1}$$

where $f(\left[Ca^{2+}\right])$ is the measured $(\Delta F/F_0)_{h\nu}$ or fluorescence intensity, $F_{\max}$ is the maximal value, F_{diff} is the difference between the the minimal and maximal value, h is the Hill coefficient, and K_d is the dissociation constant.

Analysis of the Ca^{2+} titration in HeLa cells: F_0 and F_{end} were obtained from background-corrected average intensity traces of selected cells, and were used to calculate the $(\Delta F/F_0)_{h\nu}$ values. Titration curves of the individual cells are plotted as $(\Delta F/F_0)_{h\nu}$ as a function of $\left[Ca^{2+}\right]$.

Analysis of the histamine-induced Ca^{2+}-oscillations: F_0 and F_{end} were obtained from background-corrected average intensity traces of selected cells, and were used to calculate $(\Delta F/F_0)_{h\nu}$ values. In the graphs, the black curve (fluorescence intensity) corresponds to F_0, and the red curve corresponds to $(\Delta F/F_0)_{h\nu}$. The $\left[Ca^{2+}\right]$ (green curve) is calculated by using the *in vitro* titration curve measured using the exact same settings. Values in the lowest and highest 5% of the titration curve are defined as out of the working range (as explained in figure 3), and are therefore plotted as red dots. Values within the working range are shown in green.

iPEAQ imaging: The data was split into two subsets: one subset containing the calibration photoswitching cycles, which are analyzed as described before, and a second subset with the fluorescence signal F_0. Both Ca^{2+} titration curves from the *in vitro* data, one for $(\Delta F/F_0)_{h\nu}$ and one for F_0, are taken into account for the translation into $[Ca^{2+}]$. The Ca^{2+} values gained from $(\Delta F/F_0)_{h\nu}$, are the 'calibration reference points' and F_0 is used to interpolate between these reference points. To translate F_0 into changes in $\left[Ca^{2+}\right]$, the reference Ca^{2+} values of the two calibration points encasing these data points are used to find the position on the F_0 titration curve. This calibrates the relation between the fluorescence changes and $\left[Ca^{2+}\right]$ so the intermittent F_0 points can be used to determine $\left[Ca^{2+}\right]$. We found that the first fluorescence acquisition after each switching cycle showed slight deviations, most likely due to the formation of a transient non-fluorescent intermediate that is not fully relaxed within 2 s, but does disappear after 4 s. This effect could be corrected

through reference measurements if required, but we have instead opted to replace this first point with a linearly interpolated value between the preceding and following data points since this did not appreciably change the resulting Ca^{2+} traces.

References

1. Miyawaki, A. & Niino, Y. Molecular Spies for Bioimaging-Fluorescent Protein-Based Probes. *Molecular Cell* **58,** 632–643. http://dx.doi.org/10.1016/j.molcel.2015.03.002 (2015).
2. Greenwald, E. C., Mehta, S. & Zhang, J. Genetically encoded fluorescent biosensors illuminate the spatiotemporal regulation of signaling networks. *Chemical Reviews* **118,** 11707–11794 (2018).
3. Moeyaert, B. & Dedecker, P. Genetically encoded biosensors based on innovative scaffolds. *The International Journal of Biochemistry & Cell Biology,* 105761. https://linkinghub.elsevier.com/retrieve/pii/S1357272520300789 (2020) (2020).
4. Gautier, A. & Tebo, A. G. Sensing cellular biochemistry with fluorescent chemical–genetic hybrids. *Current Opinion in Chemical Biology* **57,** 58–64. https://linkinghub.elsevier.com/retrieve/pii/S1367593120300429 (2020) (2020).
5. Palmer, A. E. & Tsien, R. Y. Measuring calcium signaling using genetically targetable fluorescent indicators. *Nature Protocols* **1,** 1057–1065 (2006).
6. Salonikidis, P. S., Zeug, A., Kobe, F., Ponimaskin, E. & Richter, D. W. Quantitative measurement of cAMP concentration using an exchange protein directly activated by a cAMP-based FRET-sensor. *Biophysical Journal* **95,** 5412–5423 (2008).
7. Park, J. G. & Palmer, A. E. in *Fluorescent Protein-Based Biosensors* (eds Zhang, J., Ni, Q. & Newman, R. H.) Series Title: Methods in Molecular Biology, 29–47 (Humana Press, Totowa, NJ, 2014). http://link.springer.com/10.1007/978-1-62703-622-1_3 (2020).
8. Palmer, A. E., Qin, Y., Park, J. G. & McCombs, J. E. Design and application of genetically encoded biosensors. *Trends in Biotechnology* **29,** 144–152. http://dx.doi.org/10.1016/j.tibtech.2010.12.004 (2011).
9. Stamatakis, A. M. *et al.* Simultaneous optogenetics and cellular resolution calcium imaging during active behavior using a miniaturized microscope. *Frontiers in Neuroscience* **12,** 1–16 (2018).
10. Miesenböck, G., De Angelis, D. A. & Rothman, J. E. Visualizing secretion and synaptic transmission with pH-sensitive green fluorescent proteins. *Nature* **394,** 192–195. http://www.nature.com/articles/BF28190 (2020) (1998).
11. Grynkiewicz, G., Poenie, M. & Tsien, R. Y. A new generation of Ca2+ indicators with greatly improved fluorescence properties. *The Journal of biological chemistry* **260,** 3440–50. http://www.ncbi.nlm.nih.gov/pubmed/3838314 (1985).
12. Dedecker, P., De Schryver, F. C. & Hofkens, J. Fluorescent Proteins: Shine on, You Crazy Diamond. *Journal of the American Chemical Society* **135,** 2387–2402. https://pubs.acs.org/doi/10.1021/ja309768d (2019) (2013).
13. Berlin, S. *et al.* Photoactivatable genetically encoded calcium indicators for targeted neuronal imaging. *Nature Methods* **12,** 852–858 (2015).
14. Ai, M. *et al.* Green-to-red photoconversion of GCaMP. *PLoS ONE* **10,** 1–11 (2015).
15. Fosque, B. F. *et al.* Labeling of active neural circuits in vivo with designed calcium integrators. *Science* **347,** 755–760. http://www.sciencemag.org/cgi/doi/10.1126/science.1260922 (2015).
16. Moeyaert, B. *et al.* Improved methods for marking active neuron populations. *Nature Communications* **9,** 4440. http://www.nature.com/articles/s41467-018-06935-2 (2020) (2018).
17. Ando, R. Regulated Fast Nucleocytoplasmic Shuttling Observed by Reversible Protein Highlighting. *Science* **306,** 1370–1373. http://dx.doi.org/10.1126/science.1102506 (2004).

18. Hofmann, M., Eggeling, C., Jakobs, S. & Hell, S. W. Breaking the diffraction barrier in fluorescence microscopy at low light intensities by using reversibly photoswitchable proteins. *Proceedings of the National Academy of Sciences* **102,** 17565–17569. http://dx.doi.org/10.1073/pnas.0506010102 (2005).
19. Habuchi, S. *et al.* Reversible single-molecule photoswitching in the GFP-like fluorescent protein Dronpa. *Proceedings of the National Academy of Sciences* **102,** 9511–9516. http://www.pnas.org/cgi/doi/10.1073/pnas.0500489102 (2020) (2005).
20. Dedecker, P. *et al.* Subdiffraction Imaging through the Selective Donut-Mode Depletion of Thermally Stable Photoswitchable Fluorophores: Numerical Analysis and Application to the Fluorescent Protein Dronpa. *Journal of the American Chemical Society* **129,** 16132–16141. https://pubs.acs.org/doi/10.1021/ja076128z (2020) (2007).
21. Shroff, H. *et al.* Dual-color superresolution imaging of genetically expressed probes within individual adhesion complexes. *Proceedings of the National Academy of Sciences* **104,** 20308–20313. http://www.pnas.org/cgi/doi/10.1073/pnas.0710517105 (2020) (2007).
22. Grotjohann, T. *et al.* Diffraction-unlimited all-optical imaging and writing with a photochromic GFP. *Nature* **478,** 204–208. http://www.nature.com/articles/nature10497 (2019) (2011).
23. Rego, E. H. *et al.* Nonlinear structured-illumination microscopy with a photoswitchable protein reveals cellular structures at 50-nm resolution. *Proceedings of the National Academy of Sciences* **109,** E135–E143. http://www.pnas.org/cgi/doi/10.1073/pnas.1107547108 (2020) (2012).
24. Dedecker, P., Mo, G. C. H., Dertinger, T. & Zhang, J. Widely accessible method for superresolution fluorescence imaging of living systems. *Proceedings of the National Academy of Sciences of the United States of America* **109,** 10909–10914 (2012).
25. Pennacchietti, F. *et al.* Fast reversibly photoswitching red fluorescent proteins for live-cell RESOLFT nanoscopy. *Nature Methods* **15,** 601–604. http://www.nature.com/articles/s41592-018-0052-9 (2020) (2018).
26. De Zitter, E. *et al.* Mechanistic investigation of mEos4b reveals a strategy to reduce track interruptions in sptPALM. *Nature Methods* **16,** 707–710. http://www.nature.com/articles/s41592-019-0462-3 (2020) (2019).
27. Duan, C., Adam, V., Byrdin, M. & Bourgeois, D. in *Photoswitching Proteins* (ed Cambridge, S.) Series Title: Methods in Molecular Biology, 177–202 (Springer New York, New York, NY, 2014). http://link.springer.com/10.1007/978-1-4939-0470-9_12 (2020).
28. Jares-Eruman, E. A., Song, L. & Jovin, T. M. Photochromism-Fret (phFRET): Modulation of Fluorescence Resonance Energy Transfer by A Photochromic Acceptor. *Molecular Crystals and Liquid Crystals Science and Technology. Section A. Molecular Crystals and Liquid Crystals* **298,** 151–159. https://www.tandfonline.com/doi/full/10.1080/10587259708036155 (2020) (1997).
29. Mao, S. *et al.* Optical Lock-In Detection of FRET Using Synthetic and Genetically Encoded Optical Switches. *Biophysical Journal* **94,** 4515–4524. https://linkinghub.elsevier.com/retrieve/pii/S0006349508701061 (2020) (2008).
30. Uphoff, S. *et al.* Monitoring multiple distances within a single molecule using switchable FRET. *Nature Methods* **7,** 831–836. http://www.nature.com/articles/nmeth.1502 (2020) (2010).
31. Rainey, K. H. & Patterson, G. H. Photoswitching FRET to monitor protein–protein interactions. *Proceedings of the National Academy of Sciences* **116,** 864–873. http://www.pnas.org/lookup/doi/10.1073/pnas.1805333116 (2020) (2019).
32. Ojha, N., Rainey, K. H. & Patterson, G. H. Imaging of fluorescence anisotropy during photoswitching provides a simple readout for protein self-association. *Nature Communications* **11,** 21. http://www.nature.com/articles/s41467-019-13843-6 (2020) (2020).

33. Golovina, V. A. & Blaustein, M. P. Spatially and functionally distinct Ca2+ stores in sarcoplasmic and endoplasmic reticulum. *Science* **275,** 1643–1648 (1997).
34. Russell, J. T. Imaging calcium signals in vivo: A powerful tool in physiology and pharmacology. *British Journal of Pharmacology* **163,** 1605–1625 (2011).
35. Lin, M. Z. & Schnitzer, M. J. Genetically encoded indicators of neuronal activity. *Nature neuroscience* **19,** 1142–53. http://www.ncbi.nlm.nih.gov/pubmed/27571193 (2016).
36. Girven, K. S. & Sparta, D. R. Probing Deep Brain Circuitry: New Advances in in Vivo Calcium Measurement Strategies. *ACS Chemical Neuroscience* **8,** 243–251 (2017).
37. Cho, J.-H. *et al.* The GCaMP-R Family of Genetically Encoded Ratiometric Calcium Indicators. *ACS Chemical Biology* **12,** 1066–1074. https://pubs.acs.org/doi/10.1021/acschembio.6b00883 (2020) (2017).
38. Akerboom, J. *et al.* Genetically encoded calcium indicators for multi-color neural activity imaging and combination with optogenetics. *Frontiers in molecular neuroscience* **6,** 2. http://www.pubmedcentral.nih.gov/articlerender.fcgi?artid=3586699 (2013).
39. Sha, F., Abdelfattah, A. S., Patel, R. & Schreiter, E. R. *rsCaMPARI: an erasable marker of neuronal activity* preprint (Neuroscience, 2019). http://biorxiv.org/lookup/doi/10.1101/798298 (2020).
40. Dana, H. *et al.* High-performance calcium sensors for imaging activity in neuronal populations and microcompartments. *Nature Methods* **16,** 649–657. http://dx.doi.org/10.1038/s41592-019-0435-6 (2019).
41. Ohkura, M., Matsuzaki, M., Kasai, H., Imoto, K. & Nakai, J. Genetically Encoded Bright Ca^{2+} Probe Applicable for Dynamic Ca^{2+} Imaging of Dendritic Spines. *Analytical Chemistry* **77,** 5861–5869. https://pubs.acs.org/doi/10.1021/ac0506837 (2019) (2005).
42. Hoi, H., Matsuda, T., Nagai, T. & Campbell, R. E. Highlightable Ca^{2+} Indicators for Live Cell Imaging. *Journal of the American Chemical Society* **135,** 46–49. https://pubs.acs.org/doi/10.1021/ja310184a (2019) (2013).
43. Barnett, L. M., Hughes, T. E. & Drobizhev, M. Deciphering the molecular mechanism responsible for GCaMP6m's Ca2+-dependent change in fluorescence. *PloS One* **12,** e0170934 (2017).
44. Grotjohann, T. *et al.* rsEGFP2 enables fast RESOLFT nanoscopy of living cells. *eLife* **1,** e00248. https://elifesciences.org/articles/00248 (2019) (2012).
45. Duwé, S. *et al.* Expression-Enhanced Fluorescent Proteins Based on Enhanced Green Fluorescent Protein for Super-resolution Microscopy. *ACS Nano* **9,** 9528–9541 (2015).
46. El Khatib, M., Martins, A., Bourgeois, D., Colletier, J.-P. & Adam, V. Rational design of ultrastable and reversibly photoswitchable fluorescent proteins for super-resolution imaging of the bacterial periplasm. *Scientific Reports* **6,** 18459 (2016).
47. Tian, L. *et al.* Imaging neural activity in worms, flies and mice with improved GCaMP calcium indicators. *Nature Methods* **6,** 875–881. http://www.nature.com/articles/nmeth.1398 (2020) (2009).
48. Chen, T.-W. *et al.* Ultrasensitive fluorescent proteins for imaging neuronal activity. *Nature* **499,** 295–300 (2013).
49. Zhao, Y. *et al.* An Expanded Palette of Genetically Encoded Ca2+ Indicators. *Science* **333,** 1888–1891. https://www.sciencemag.org/lookup/doi/10.1126/science.1208592 (2020) (2011).
50. Pédelacq, J.-D., Cabantous, S., Tran, T., Terwilliger, T. C. & Waldo, G. S. Engineering and characterization of a superfolder green fluorescent protein. *Nature biotechnology* **24,** 79–88. http://www.ncbi.nlm.nih.gov/pubmed/16369541 (2006).

51. Muto, A. *et al.* Genetic visualization with an improved GCaMP calcium indicator reveals spatiotemporal activation of the spinal motor neurons in zebrafish. *Proceedings of the National Academy of Sciences* **108,** 5425–5430. http://www.pnas.org/cgi/doi/10.1073/pnas.1000887108 (2020) (2011).
52. Akerboom, J. *et al.* Optimization of a GCaMP Calcium Indicator for Neural Activity Imaging. *Journal of Neuroscience* **32,** 13819–13840. http://www.jneurosci.org/cgi/doi/10.1523/JNEUROSCI.2601-12.2012 (2020) (2012).
53. Brakemann, T. *et al.* Molecular basis of the light-driven switching of the photochromic fluorescent protein Padron. *The Journal of Biological Chemistry* **285,** 14603–14609 (2010).
54. Nienhaus, K. & Nienhaus, G. U. Photoswitchable Fluorescent Proteins: Do Not Always Look on the Bright Side. *ACS Nano* **10,** 9104–9108. https://pubs.acs.org/doi/10.1021/acsnano.6b06298 (2020) (2016).
55. Bootman, M. D. & Berridge, M. J. Subcellular Ca^{2+} signals underlying waves and graded responses in HeLa cells. *Current Biology* **6,** 855–865. https://linkinghub.elsevier.com/retrieve/pii/S0960982202006097 (2020) (1996).
56. Carter, K. P., Carpenter, M. C., Fiedler, B., Jimenez, R. & Palmer, A. E. Critical Comparison of FRET-Sensor Functionality in the Cytosol and Endoplasmic Reticulum and Implications for Quantification of Ions. *Analytical Chemistry* **89,** 9601–9608. http://dx.doi.org/10.1021/acs.analchem.7b02933 (2017).
57. Sawano, A. & Miyawaki, A. Directed evolution of green fluorescent protein by a new versatile PCR strategy for site-directed and semi-random mutagenesis. *Nucleic acids research* **28,** E78 (2000).
58. Ai, H.-w., Baird, M. A., Shen, Y., Davidson, M. W. & Campbell, R. E. Engineering and characterizing monomeric fluorescent proteins for live-cell imaging applications. *Nature Protocols* **9,** 910–928. http://www.nature.com/articles/nprot.2014.054 (2020) (2014).
59. Moeyaert, B. *et al.* Green-to-Red Photoconvertible Dronpa Mutant for Multimodal Super-resolution Fluorescence Microscopy. *ACS Nano* **8,** 1664–1673. (2018) (2014).
60. Ward, W. Properties of the Coelenterate green-fluorescent proteins. *Bioluminescence and Chemiluminescence: Basic Chemistry and Analytical applications. Eds. DeLuca, M. & McElroy, WD (Academic Press, Inc., NY),* 235–242 (1981).
61. Tsien, R. The green fluorescent protein. *Annual Review of Biochemistry* **67,** 509–544 (1998).